Seventh International Conference on
Computational Fluid Dynamics (ICCFD7),
Big Island, Hawaii, July 9-13, 2012

ICCFD7-4202

High-order Discontinuous Galerkin Methods for Turbulent High-lift Flows

Nicholas K. Burgess[*] and Dimitri J. Mavriplis[+]
Corresponding author: nicholas.k.burgess.ctr@us.army.mil

[*] Science and Technology Corporation, Moffett Field CA, USA
[+] Department of Mechanical Engineering University of Wyoming, Laramie WY, USA.

July 16, 2012

Abstract: In this work a robust discontinuous Galerkin (DG) solver for turbulent high-lift aerodynamic flows using the turbulence model of Spalart and Allmaras (SA) is developed. The application of DG discretizations to turbulent RANS flows is one of the most pressing issues facing high-order methods on unstructured grids. The issue is the result of non-smooth behavior of the turbulence model equation, which often causes solver failure for high-order discretizations. Herein a modification to the turbulence model of Spalart and Allmaras is implemented within a DG-based unstructured CFD solver for the RANS equations and utilized to compute high-lift aerodynamic flows. Additionally, the convective discretization of the SA turbulence model equation as it relates to solver robustness is discussed at length.

Keywords: High-Order Methods, Computational Fluid Dynamics, Turbulence Modeling.

1 Introduction

High-order discontinuous Galerkin (DG) methods are now an abundant topic in the Computational Fluid Dynamics (CFD) literature. These methods have been successfully applied to the Euler and laminar Navier-Stokes equations [1, 2, 3, 4, 5, 6] with excellent accuracy properties. Initially high-order discontinuous Galerkin (DG) methods were applied to smooth problems due to the inherent difficulties with computing discontinuous solutions via high-order DG methods. However, recent work has demonstrated that high-order DG methods can be use to compute flows with shockwaves[7, 8, 9, 10, 11, 12, 13, 14, 15, 16]. While the ability to robustly and accurately resolve flows with discontinuities is a significant leap towards the general adoption of DG methods for use in CFD solvers, one major stumbling block remains: turbulence modeling.

Recent research[17, 18, 19, 20, 21] into the robust application of DG methods to the Reynolds Averaged Navier-Stokes (RANS) equations has proven difficult, due to non-smooth solution behavior of the turbulence modeling equations. In particular, this work considers the solution of the Spalart Allmaras (SA) turbulence model[22]. Recent work[19] has shown that the non-smooth behavior of the SA turbulence model often causes solver failure. In the authors' experience the this is especially true for high-lift applications. Solver failure is the result of negative values of the SA working variable. These negative values are generated by Gibbs phenomena that result from employing high-order approximations across a discontinuity. Over the last few years several researchers[17, 23, 18, 21] have proposed a variety of techniques to alleviate the solver difficulties that arise from non-smooth behavior of the SA turbulence model. However, it was not until recently that Moro et al[20] presented a modification to the SA turbulence model that significantly improved the robustness of high-order discretizations. This modification does not remove the non-smooth behavior, rather the modification seeks to make the effects of non-smooth behavior benign. It is also

Seventh International Conference on
Computational Fluid Dynamics (ICCFD7),
Big Island, Hawaii, July 9-13, 2012

ICCFD7-4202

worth mentioning that modifications to the turbulence model are not the only requirement for a robust and accurate high-order DG solver. Recent work [24, 21] has demonstrated that the effects of convective flux treatment and implicit solver formulation are significant.

Although the use of high-order accurate discretizations for RANS problems is not commonplace, there are several examples of successful high-order DG RANS solutions using standard turbulence models in the literature [25, 17, 23, 19, 26]. The current solver using a DG discretization of the standard Spalart-Allmaras (SA) turbulence model [22] has been able to replicate almost all the results of these references, however not as robustly as is required for production use. Additionally, high-lift flows consisting of both single and multiple airfoils, have proven to be the most difficult cases to solve. Therefore, in order to develop a high-order DG solver that is capable of solving such flows, one must consider all aspects of defining and discretizing the SA turbulence model equation.

A robust high-order DG solver for turbulent flows requires some key ingredients related to the form and discretization of the turbulence model equation. This work describes the turbulence model: definition, discretization and implicit solution techniques that make the present high-order DG solver robust enough to compute high-lift turbulent flows. The robustness of the proposed approach is demonstrated by considering challenging high-lift flows.

2   Governing Equations

The conservative form of the compressible Reynolds Averaged Navier-Stokes (RANS) equations describing the conservation of mass, momentum and total energy in two dimensions are given as:

$$\frac{\partial \mathbf{u}}{\partial t} + \nabla \cdot \left(\vec{\mathbf{F}}_c(\mathbf{u}) - \vec{\mathbf{F}}_v(\mathbf{u}, \nabla \mathbf{u}) \right) = \mathbf{S}(\mathbf{u}, \nabla \mathbf{u}) \tag{1}$$

subject to the appropriate boundary and initial conditions within a domain Ω. In this work the RANS equations are coupled to the one equation turbulence model of Spalart and Allmaras (SA model)[22] with the modifications given in references [23, 20]. The equation for this model is given by:

$$\frac{\partial \rho \tilde{v}}{\partial t} + \nabla \cdot (\rho \tilde{v} \vec{v}) = c_{b_1} \tilde{S} \rho v \psi + \frac{1}{\sigma} \left[\nabla \cdot \left((\mu + \mu \psi) \nabla \tilde{v} \right) + c_{b_2} \rho \nabla \tilde{v} \cdot \nabla \tilde{v} \right] - c_{w_1} \rho f_w \left(\frac{v \psi}{d} \right)^2 \tag{2}$$

where $\tilde{S}$ is given according to

$$\tilde{S} = \begin{cases} S + \bar{S} & \bar{S} \geq -c_{v_2} S \\ S + \frac{S \left(c_{v_2}^2 S + c_{v_3} \bar{S} \right)}{(c_{v_3} - 2 c_{v_2}) S - \bar{S}} & \bar{S} \leq -c_{v_2} S \end{cases} \tag{3}$$

$$S = \sqrt{\vec{\omega} \cdot \vec{\omega}}$$

$$\bar{S} = \frac{(v \psi)^2 f_{v_2}}{\kappa^2 d^2} \tag{4}$$

where $\vec{\omega}$ is the vorticity vector. The f_{v_2} function is given as:

$$f_{v_2} = 1 - \frac{\psi}{1 + \psi f_{v_1}} \tag{5}$$

and the destruction term coefficients are given by:

$$r = \frac{v \psi}{\tilde{S} \kappa^2 d^2}$$

$$g = r + c_{w_2} \left(r^6 - r \right)$$

$$f_w = g \left[\frac{1 + c_{w_3}^6}{g^6 + c_{w_3}^6} \right]^{1/6} \tag{6}$$

The constants c_{b_1}, c_{v_1}, κ, etc. are the same as those in reference [22]. The additional constant c_{v_3} is given as $c_{v_3} = .9$. The variable ψ is designed to remain positive regardless of the value of $\tilde{v}$ and is given by:

$$\psi = \begin{cases} .05 log \left(1.0 + e^{(20.0\chi)} \right) & \chi \leq 10.0 \\ \chi & \chi > 10.0 \end{cases}$$

$$\chi = \frac{\tilde{v}}{v}$$

(7)

The use of the variable ψ proposed in reference [20] is simple to implement within an existing CFD solver and is also easy to differentiate for implicit solution techniques. The effect of the modification is to deactivate the production, destruction and diffusion terms of the turbulence model equation when $\tilde{v}$ becomes negative, effectively rendering it as a simple advection equation, which is unaffected by negative values of $\tilde{v}$. While employing the variable ψ in the model source terms comes directly from reference[20], this reference does not use the modified form of $\tilde{S}$, which in the authors' experience provides addition robustness to the turbulence model equation in the positive $\tilde{v}$ regime.

The state vector and flux vectors including those of the SA model equation for two-dimensional flow are explicitly given as:

$$\mathbf{u} = \begin{Bmatrix} \rho \\ \rho u \\ \rho v \\ E_t \\ \rho \tilde{v} \end{Bmatrix}, \quad \mathbf{F_c}^x = \begin{Bmatrix} \rho u \\ \rho u^2 + P \\ \rho u v \\ u(E_t + P) \\ \rho u \tilde{v} \end{Bmatrix}, \quad \mathbf{F_c}^y = \begin{Bmatrix} \rho v \\ \rho u v \\ \rho v^2 + P \\ v(E_t + P) \\ \rho v \tilde{v} \end{Bmatrix},$$

$$\mathbf{F_v}^x = \begin{Bmatrix} 0 \\ \tau_{xx} \\ \tau_{xy} \\ u\tau_{xx} + v\tau_{xy} + c_p \left(\frac{\mu}{Pr} + \frac{\mu_T}{Pr_T} \right) \frac{\partial T}{\partial x} \\ \frac{1}{\sigma} (\mu + \mu\psi) \frac{\partial \tilde{v}}{\partial x} \end{Bmatrix}, \quad \mathbf{F_v}^y = \begin{Bmatrix} 0 \\ \tau_{yx} \\ \tau_{yy} \\ u\tau_{yx} + v\tau_{yy} + c_p \left(\frac{\mu}{Pr} + \frac{\mu_T}{Pr_T} \right) \frac{\partial T}{\partial y} \\ \frac{1}{\sigma} (\mu + \mu\psi) \frac{\partial \tilde{v}}{\partial y} \end{Bmatrix},$$

(8)

$$\mathbf{S} = \begin{Bmatrix} 0 \\ 0 \\ 0 \\ 0 \\ c_{b_1} \tilde{S} \rho v \psi + \frac{1}{\sigma} [c_{b_2} \rho \nabla \tilde{v} \cdot \nabla \tilde{v}] - c_{w_1} \rho f_w \left(\frac{v\psi}{d} \right)^2 \end{Bmatrix}$$

where ρ is fluid density, $\vec{u} = (u, v)$ are the Cartesian velocity components, P is the fluid pressure, E_t is the total energy, c_p is the specific heat at constant pressure, T is the fluid temperature, P_r and P_{rT} are the Prandtl and turbulent Prandtl numbers respectively and τ_{ij} is the total viscous stress tensor including the Boussinesq approximated Reynolds stresses. Assuming a Newtonian fluid and using the Boussinesq approximation for the Reynolds stresses, the viscous stress tensor takes the form (with $x_i = x, y; \quad i = 1, 2$):

$$\tau_{ij} = 2 (\mu + \mu_T) S_{ij}$$

$$S_{ij} = \frac{1}{2} \left(\frac{\partial u_i}{\partial x_j} + \frac{\partial u_j}{\partial x_i} \right) - \frac{1}{3} \frac{\partial u_k}{\partial x_k} \delta_{ij}$$

$$\text{for } i = 1, 2, j = 1, 2$$

(9)

Seventh International Conference on
Computational Fluid Dynamics (ICCFD7),
Big Island, Hawaii, July 9-13, 2012

ICCFD7-4202

where μ is the fluid viscosity obtained via Sutherland's law and μ_T is a turbulent eddy viscosity, which is given by:

$$
\mu_T = \begin{cases} \rho \tilde{v} f_{v_1} & \tilde{v} \geq 0 \\ 0 & \tilde{v} < 0 \end{cases}
$$

$$
f_{v_1} = \frac{\left(\frac{\rho \tilde{v}}{\mu}\right)^3}{\left(\frac{\rho \tilde{v}}{\mu}\right)^3 + c_{v_1}^3} \tag{10}
$$

$$
c_{v_1} = 7.1
$$

The components of the viscous stress tensor for two dimensional flow are given explicitly as:

$$
\tau_{xx} = (\mu + \mu_T)\left(\frac{4}{3}\frac{\partial u}{\partial x} - \frac{2}{3}\frac{\partial v}{\partial y}\right), \quad \tau_{xy} = (\mu + \mu_T)\left(\frac{\partial u}{\partial y} + \frac{\partial v}{\partial x}\right)
$$

$$
\tau_{yx} = (\mu + \mu_T)\left(\frac{\partial u}{\partial y} + \frac{\partial v}{\partial x}\right), \quad \tau_{yy} = (\mu + \mu_T)\left(\frac{4}{3}\frac{\partial v}{\partial y} - \frac{2}{3}\frac{\partial u}{\partial x}\right) \tag{11}
$$

It should be understood that all quantities in the above equations are the Reynolds Averaged quantities (the usual $\bar{(\,)}$ notation is omitted for simplicity). The pressure is obtained from the ideal gas equation of state given as:

$$
P = (\gamma - 1)\left[E_t - \frac{1}{2}\rho\left(u^2 + v^2\right)\right] \tag{12}
$$

where $\gamma = 1.4$ is the ratio of specific heats.

The DG discretization used in this work is detailed in reference[21] and will not be repeated herein. The interested reader is encouraged to examine reference[21] for a highly detailed description of the DG discretization employed in this work.

3 Roe's Riemann Solver for RANS-SA System

Solving the Reynolds Averaged Navier-Stokes (RANS) equations requires the discretization of one or more turbulence model equations. In this work, the one-equation turbulence model of Spalart and Allmaras (SA)[22] is used to close the RANS equations. Many production level solvers[27, 28, 29, 30] view the discretization of the turbulence model in a decoupled fashion, which results in treating the convection term as though it were a scalar transport equation evolving with a prescribed velocity field. However, this treatment neglects the fact that the velocity field, which convects the turbulence model quantities, is heavily influenced by the turbulence model solution. Therefore, in this work the turbulence model used to close the RANS equations is fully coupled to the mean flow equations and the RANS-SA system is considered as a complete system of equations. This treatment necessitates re-deriving the convective numerical flux function to include the turbulence model equation.

The RANS equations closed with the SA turbulence model results in a total of five equations in two spatial dimensions. In order to produce a stable and accurate convective discretization, the numerical flux function must be derived for the convective terms of the five coupled equations. Consider the convective flux vectors, originally given in equation (8), labeled as $\mathbf{F}_c$. Considering these flux vectors, the method of Roe and Pike[31] is used to derive a numerical flux function for the coupled RANS-SA system. The method of Roe and Pike requires the eigenvalues and eigenvectors of the Jacobian of the convective flux normal to an interface. The normal flux $\mathbf{F_c}^n$ is given by:

$$
\mathbf{F_c}^n = \begin{Bmatrix} \rho u n_x + \rho v n_y \\ \left(\rho u^2 + P\right)n_x + \rho u v n_y \\ \rho u v n_x + \left(\rho v^2 + P\right)n_y \\ u(E_t + P)n_x + v(E_t + P)n_y \\ \rho u \tilde{v} n_x + \rho v \tilde{v} n_y \end{Bmatrix} \tag{13}
$$

Seventh International Conference on
Computational Fluid Dynamics (ICCFD7),
Big Island, Hawaii, July 9-13, 2012

ICCFD7-4202

The eigenvalues λ and eigenvectors K of the fully coupled RANS-SA convective flux Jacobian are:

$$\lambda_1 = \vec{u}\cdot\vec{n} - a \quad \lambda_2 = \vec{u}\cdot\vec{n} \quad \lambda_3 = \vec{u}\cdot\vec{n} \quad \lambda_4 = \vec{u}\cdot\vec{n} \quad \lambda_5 = \vec{u}\cdot\vec{n} + a$$

$$K_1 = \left\{ \begin{array}{c} 1 \\ u - an_x \\ v - an_y \\ H - \vec{u}\cdot\vec{n}a \\ s \end{array} \right\}, K_2 = \left\{ \begin{array}{c} 1 \\ u \\ v \\ \frac{1}{2}\left(u^2 + v^2\right) \\ 0 \end{array} \right\}, K_3 = \left\{ \begin{array}{c} 0 \\ -n_y \\ n_x \\ -un_y + vn_x \\ 0 \end{array} \right\},$$

$$K_4 = \left\{ \begin{array}{c} 0 \\ 0 \\ 0 \\ 0 \\ 1 \end{array} \right\}, K_5 = \left\{ \begin{array}{c} 1 \\ u + an_x \\ v + an_y \\ H + \vec{u}\cdot\vec{n}a \\ s \end{array} \right\},$$

$$(14)$$

where $\vec{u} = (u,v)$ are the Cartesian velocity components, $\vec{n} = (n_x, n_y)$ is the surface normal vector, a is the sound speed, H is the total enthalpy, and s is the scalar, which would be $\tilde{v}$ for the SA turbulence model equation.

Following reference[31] the numerical flux at the interface, given by the Roe and Pike method, $\mathcal{H}_c$ is written as:

$$\mathcal{H}_c\left(\mathbf{u}^+, \mathbf{u}^-\right) = \frac{1}{2}\left(\mathbf{F_c}^n\left(\mathbf{u}^+\right) + \mathbf{F_c}^n\left(\mathbf{u}^-\right) + \sum_i \tilde{\alpha}_i \left|\tilde{\lambda}_i\right| \tilde{K}_i \left(\mathbf{u}^+ - \mathbf{u}^-\right) \right) \tag{15}$$

This expression requires the determination of the wave strength coefficients $\tilde{\alpha}_i$ and the Roe state $\tilde{()}$, which are determined using the following formulas:

$$\Delta \mathbf{u} = \left(\mathbf{u}^+ - \mathbf{u}^-\right) = \sum_i \tilde{\alpha}_i \tilde{K}_i$$

$$\Delta \mathbf{F_c}^n = \mathbf{F_c}^n\left(\mathbf{u}^+\right) - \mathbf{F_c}^n\left(\mathbf{u}^-\right) = \sum_i \tilde{\alpha}_i \tilde{\lambda}_i \tilde{K}_i \tag{16}$$

evaluated to $O\left(\Delta^2\right)$. For example, it is easy to see that

$$\Delta\left(\rho u\right) = \tilde{u}\Delta\rho + \tilde{\rho}\Delta u + O\left(\Delta^2\right) \tag{17}$$

To $O\left(\Delta^2\right)$, the wave strength coefficients are determined by solving the following system of equations:

$$\left\{ \begin{array}{c} \tilde{\alpha}_1 + \tilde{\alpha}_2 + \tilde{\alpha}_5 = \Delta\rho \\ \tilde{\alpha}_1\left(\tilde{u} - \tilde{a}n_x\right) + \tilde{\alpha}_2 u - \tilde{\alpha}_3 n_y + \tilde{\alpha}_5\left(\tilde{u} + \tilde{a}n_x\right) = \tilde{u}\Delta\rho + \tilde{\rho}\Delta u \\ \tilde{\alpha}_1\left(\tilde{v} - \tilde{a}n_y\right) + \tilde{\alpha}_2 v - \tilde{\alpha}_3 n_x + \tilde{\alpha}_5\left(\tilde{v} + \tilde{a}n_y\right) = \tilde{v}\Delta\rho + \tilde{\rho}\Delta v \\ \tilde{\alpha}_1\left(H - \left(\tilde{u}n_x + \tilde{v}n_y\right)\tilde{a}\right) + \frac{1}{2}\tilde{\alpha}_2\left(\tilde{u}^2 + \tilde{v}^2\right) + \tilde{\alpha}_3\left(-\tilde{u}n_y + \tilde{v}n_x\right) + \\ \tilde{\alpha}_5\left(H + \left(\tilde{u}n_x + \tilde{v}n_y\right)\tilde{a}\right) = \tilde{E}\Delta\rho + \tilde{\rho}\Delta E \\ \tilde{\alpha}_1\tilde{s} + \tilde{\alpha}_4 + \tilde{\alpha}_5\tilde{s} = \tilde{s}\Delta\rho + \tilde{\rho}\Delta\tilde{s} \end{array} \right\} \tag{18}$$

The second of equation (16), which is the jump in fluxes, is evaluated using a similar approach, which results in a lengthy set of equations to solve for the $\tilde{()}$ state. The result of solving these equations is a fully specified Roe state, as well as a definition of the numerical flux function for the fully coupled RANS-SA system.

Seventh International Conference on
Computational Fluid Dynamics (ICCFD7),
Big Island, Hawaii, July 9-13, 2012

ICCFD7-4202

The Roe state for the RANS-SA system is:

$$\tilde{\rho} = \sqrt{\rho^+ \rho^-}$$

$$\tilde{u} = \frac{\sqrt{\rho^+} u^+ + \sqrt{\rho^-} u^-}{\sqrt{\rho^+} + \sqrt{\rho^-}}$$

$$\tilde{v} = \frac{\sqrt{\rho^+} v^+ + \sqrt{\rho^-} v^-}{\sqrt{\rho^+} + \sqrt{\rho^-}}$$

$$\tilde{H} = \frac{\sqrt{\rho^+} H^+ + \sqrt{\rho^-} H^-}{\sqrt{\rho^+} + \sqrt{\rho^-}} \tag{19}$$

$$\tilde{s} = \frac{\sqrt{\rho^+} s^+ + \sqrt{\rho^-} s^-}{\sqrt{\rho^+} + \sqrt{\rho^-}}$$

$$\tilde{a} = \sqrt{(\gamma - 1)\left(\tilde{H} - \frac{1}{2}\left(\tilde{u}^2 + \tilde{v}^2\right)\right)}$$

The numerical flux on the boundary can be written as:

$$\mathcal{H}_c\left(\mathbf{u}^+, \mathbf{u}^-\right) = \frac{1}{2}\left(\mathbf{F_c}^n\left(\mathbf{u}^+\right) + \mathbf{F_c}^n\left(\mathbf{u}^-\right) + \mathbf{D}\right) \tag{20}$$

where $\mathbf{D}$ is the dissipative component of the numerical flux, which is given as:

$$\mathbf{D} = \left\{ \begin{array}{c} \left|\tilde{\lambda}_2\right|\left(\rho^+ - \rho^-\right) + \delta_1 \\ \left|\tilde{\lambda}_2\right|\left(\rho u^+ - \rho u^-\right) + \delta_1 \tilde{u} + \delta_2 n_x \\ \left|\tilde{\lambda}_2\right|\left(\rho v^+ - \rho v^-\right) + \delta_1 \tilde{v} + \delta_2 n_y \\ \left|\tilde{\lambda}_2\right|\left(E_t^+ - E_t^-\right) + \delta_1 \tilde{H} + \delta_2\left(\tilde{u} n_x + \tilde{v} n_y\right) \\ \left|\tilde{\lambda}_2\right|\left(\rho s^+ - \rho s^-\right) + \delta_1 \tilde{s} \end{array} \right\}$$

$$\delta_1 = \left(-\left|\tilde{\lambda}_2\right| + \frac{\left|\tilde{\lambda}_5\right| + \left|\tilde{\lambda}_1\right|}{2}\right)\frac{\Delta P}{\tilde{a}^2} + \frac{\left|\tilde{\lambda}_5\right| - \left|\tilde{\lambda}_1\right|}{2}\frac{\tilde{\rho}}{\tilde{a}}\left(n_x \Delta u + n_y \Delta v\right) \tag{21}$$

$$\delta_2 = \left(-\left|\tilde{\lambda}_2\right| + \frac{\left|\tilde{\lambda}_5\right| + \left|\tilde{\lambda}_1\right|}{2}\right)\tilde{\rho}\left(n_x \Delta u + n_y \Delta v\right) + \frac{\left|\tilde{\lambda}_5\right| - \left|\tilde{\lambda}_1\right|}{2}\frac{\Delta P}{\tilde{a}}$$

where the term $\Delta\left(\right)$ is given by:

$$\Delta\left(\right) = \left(\right)^+ - \left(\right)^- \tag{22}$$

Comparison of the dissipation terms in equation (21) with the standard formulas given in reference[31], shows that coupling the SA turbulence model equation to the RANS system does not change the numerical flux expressions for the mean flow equations. However, if the derivation for convective flux of the SA turbulence model equation were carried out in a decoupled fashion (which is the standard approach[30, 29, 28, 21] then the dissipation term of the numerical flux for the turbulence model equation involves only the velocity normal to the surface. In essence the last component of $\mathbf{D}$ would be missing the $\delta_1 \tilde{s}$ in the standard decoupled approach. However, the present approach while not standard practice is mathematically rigorous.

While the authors do note that the omission of the $\delta_1 \tilde{s}$ has not proven problematic (in fact it is necessary to omit this term under certain circumstance[24]) for first-order finite-volume discretizations of the turbulence model, this term is deemed beneficial to solver robustness for high-order DG discretizations of the SA turbulence model equation. Furthermore, numerical experiments with various combinations of numerical fluxes for the RANS and

Seventh International Conference on
Computational Fluid Dynamics (ICCFD7),
Big Island, Hawaii, July 9-13, 2012

ICCFD7-4202

SA turbulence model equations, demonstrated that using the same numerical flux for both the RANS and turbulence model equations results in a significantly more robust solver. It is generally recommended that when turbulence models are discretized using DG methods the numerical flux formulation be treated similarly. A detailed discussion of the numerical experiments that lead to the construction and use of this formulation can be found in references[21].

4   Implicit Solution Method

In addition to stable discretizations, efficient and robust solution techniques are required for the development of a robust production level aerodynamic DG solver. In this work, the RANS-SA system is solved using a damped Newton solver that treats the mean flow and turbulence model equations in a fully coupled fashion [19, 21]. The linear solver used at each Newton step is based on a line-implicit colored Gauss-Seidel (CGS) preconditioned GMRES solver[21]. The line-implicit colored Gauss-Seidel preconditioner is employed to alleviate the stiffness associated with highly anisotropic grids and requires the construction of lines through an unstructured grid. The lines are constructed using a weighted graph approach[19]. A fully parallel Gauss-Seidel method requires coloring the lines which is accomplished via a greedy algorithm that loops over all the lines formed for the line-implicit solver, assigning color integers to the lines. Once the lines have been colored, a block-tridiagonal solver is employed in a Gauss-Seidel fashion over the colors.

Constructing implicit solution techniques requires the determination of the flow Jacobian matrix. The flow Jacobian requires the differentiation of the residual $\mathbf{R}_h$ with respect to the discrete solution $\mathbf{u}_h$, a process known as linearization. Turbulence models are often linearized in a decoupled fashion i.e. turbulence models are linearized only with respect to the variables that the model equation controls. This results in a loosely coupled implicit solver formulation, that may not be able to fully converge the discrete equations. However, if the linearization is performed in a fully coupled fashion, it is far more likely that full convergence of the discrete equations can be achieved, at least with the presented DG solver. Full convergence of the discrete equations is especially important for high-order discretizations, since the magnitude of high-order modal coefficients can be very small. A full analysis of coupled versus de-coupled linearizations was conducted in reference[24].

5   Aerodynamic Applications

5.1   NACA0012 Airfoil at $\alpha = 10^o$

The first test case is the turbulent flow over a NACA0012 airfoil at a high angle of attack. This flow is particularly challenging due to the reliance of the steady-state and attached nature of flow on the turbulence model. Furthermore, the high angle of attack makes it difficult for the grid generator to cluster the grid in the correct wake location. Grid clustering has been known to alleviate some of the difficulties encountered with negative values of $\tilde{v}$[21]. The flow conditions are $M_\infty = .15$, $\alpha = 10.0^o$ and $Re = 5,000,000$. For this test case discretization orders $p = 1$ to $p = 4$ are employed using the fixed mesh in Figure 1, which contains $N = 7,373$ elements.

Figure 2(a) and Figure 2(b) show the Mach number and eddy viscosity contours respectively. Despite the relatively short chord-wise extend of the anisotropic wake grid, the wake is well resolved by the $p = 4$ polynomials. Additionally, the eddy viscosity contours in Figure 2(b) show that the peak eddy viscosity occurs over 1 chord length downstream from the airfoil trailing edge. For airfoil flows solved using the classical approach to turbulence model discretization, the peak value of the eddy viscosity is usually just down-stream form the airfoil trailing edge[24].

Figure 3 shows the convergence histories of the RANS and SA turbulence model equations for both $p = 1$ and $p = 2$ discretizations. For this test case all higher-order solutions where initialized using low-order solutions and therefore the $p = 1$ solution is the most difficult solution to obtain, since it is initialized with free stream values. However, the solution achieves steady state as demonstrated by Figure 3. Additionally, the $p = 3$ and $p = 4$ convergence histories are similar to the $p = 2$ result.
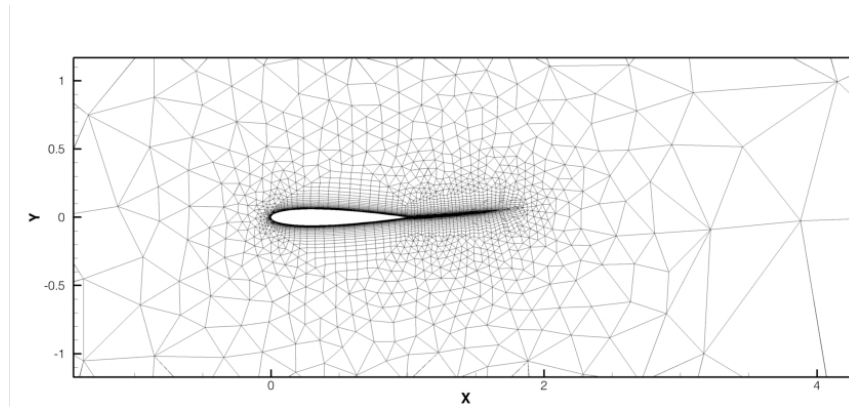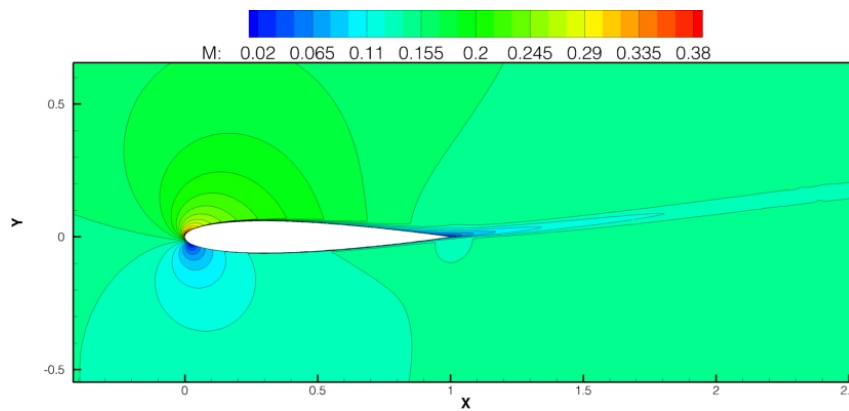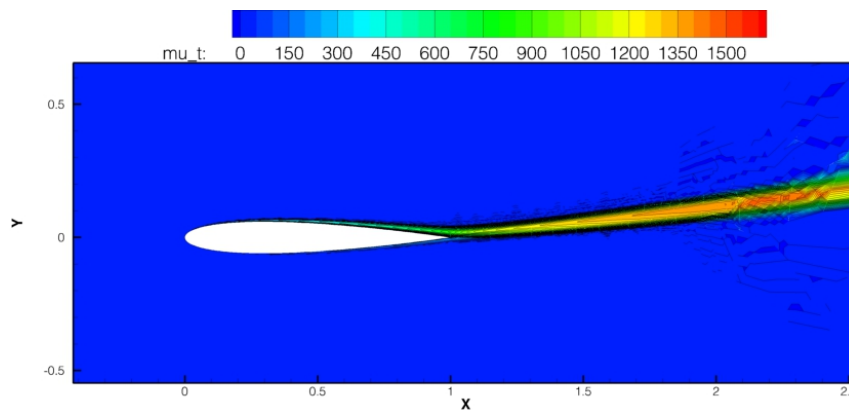
Seventh International Conference on
Computational Fluid Dynamics (ICCFD7),
Big Island, Hawaii, July 9-13, 2012

ICCFD7-4202

Figure 1: Computational mesh used for computing the flow around aNACA0012 airfoil at $M_\infty = .15$, $\alpha = 10.0^o$, and $Re = 5,000,000$.

(a) Mach number contours at $p = 4$

(b) $\frac{mu_T}{\mu\infty}$ at $p = 4$

Figure 2: Computed Mach number and eddy viscosity contours using the Spalart-Allmaras turbulence model for flow over the NACA0012 airfoil at $M_\infty = .15$, $\alpha = 10.0^o$, and $Re = 5,000,000$ using $p = 4$.

Seventh International Conference on
Computational Fluid Dynamics (ICCFD7),
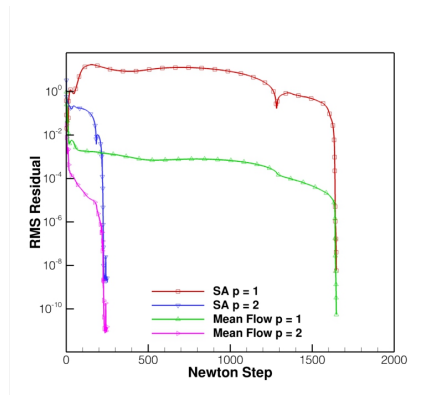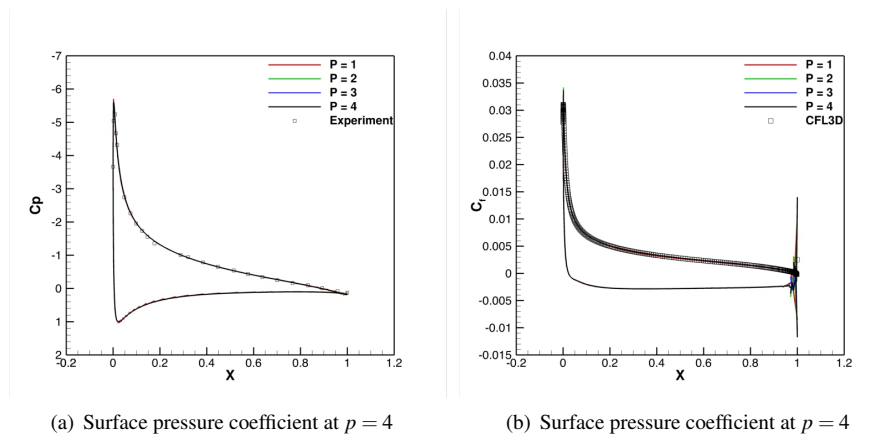**Big Island, Hawaii, July 9-13, 2012**

ICCFD7-4202

Figure 3: Convergence history of the flow around a NACA0012 airfoil at $M_\infty = .15$, $\alpha = 10.0^o$, and $Re = 5,000,000$.

(a) Surface pressure coefficient at $p = 4$

(b) Surface pressure coefficient at $p = 4$

Figure 4: Computed surface pressure and skin friction coefficients using the Spalart-Allmaras turbulence model for flow over a NACA0012 airfoil discretization orders $p = 1$ to $p = 4$, $M_\infty = .15$, $\alpha = 10.0^o$, and $Re = 5,000,000$.

9

Seventh International Conference on
Computational Fluid Dynamics (ICCFD7),
Big Island, Hawaii, July 9-13, 2012

ICCFD7-4202

Figure 4(a) shows the computed surface pressure coefficient profiles obtained using discretization orders $p = 1$ to $p = 4$. For this test case experimental data was available for comparison and is plotted alongside the computation results in Figure 4(a). The computational and experimental results are in excellent agreement. Figure 4(b) shows the computed surface skin friction coefficient along with results from the CFL3D[30] solver, since no experimental data was available for the skin friction coefficient. The agreement between the two solvers is excellent.

Close examination of the modified turbulence model shows that for small values of $\tilde{\nu}$ the model is not exactly the same as the original model, which could adversely impact the solution near the wall. However, the agreement between the results generated by CFL3D and the DG solver show that this modification does not impact the computed skin friction coefficient, which is the output that is most sensitive to slight shape perturbations in the near wall velocity profile.

Table 1: Computed lift and drag coefficients for the NACA0012 airfoil at $M_\infty = .15$, $\alpha = 10.0^o$, and $Re = 5,000,000$ using $p = 1$ to $p = 4$

p	NDoF	C_L	C_D
1	27,846	1.054429	0.014977
2	61,419	1.087564	0.014925
3	108,092	1.097283	0.014630
4	167,865	1.090325	0.012745

Table 1 shows the computed drag and lift coefficients for this case. Unfortunately there isn't an extractable trend shown by this data, a sign that the asymptotic range has not been reached despite the high polynomial degree employed.

5.2   High-lift Multi-element Airfoil Configuration L1T2

The second test case consists of the turbulent flow over the AGARD L1T2 high-lift multi-element airfoil configuration. The geometry consists of a three-element airfoil configuration and the flow conditions are $M = .197$, $\alpha = 20.18^o$, and $Re = 3,520,000$. The mesh employed for this test case is a mixed-element unstructured mesh with $N = 80,742$ elements as shown Figure 5. In this case, discretization orders ranging from $p = 1$ to $p = 4$ are employed.
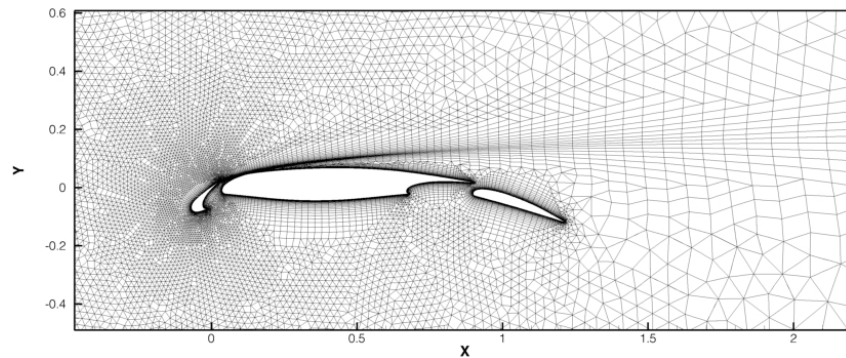

Figure 5: Computational mesh used for computing the flow around the AGARD L1T2 high-lift multi-element airfoil configuration at $M_\infty = .197$, $\alpha = 20.18^o$, and $Re = 3,520,000$.

Seventh International Conference on
Computational Fluid Dynamics (ICCFD7),
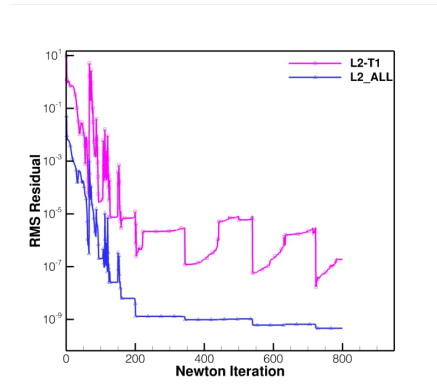**Big Island, Hawaii, July 9-13, 2012**

ICCFD7-4202

Figure 6: Convergence history of the flow around the AGARD L1T2 high-lift multi-element airfoil configuration at $M_\infty = .197$, $\alpha = 20.18^o$, and $Re = 3,520,000$.

(a) Mach number contours at $p = 4$
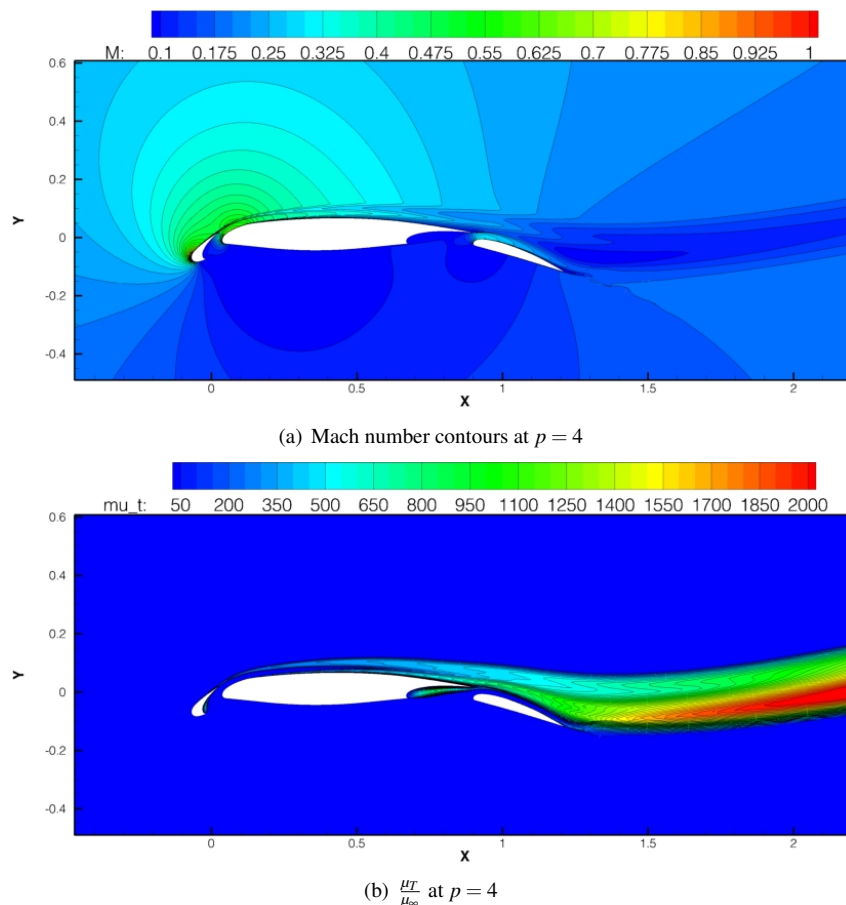

(b) $\frac{\mu_T}{\mu_\infty}$ at $p = 4$

Figure 7: Computed Mach number and eddy viscosity contours using the Spalart-Allmaras turbulence model for flow over the AGARD L1T2 high-lift multi-element airfoil configuration with $p = 4$ at $M_\infty = .197$, $\alpha = 20.18^o$, and $Re = 3,520,000$.

Seventh International Conference on
Computational Fluid Dynamics (ICCFD7),
Big Island, Hawaii, July 9-13, 2012

ICCFD7-4202

(a) Surface pressure coefficient at $p = 4$ (b) Surface pressure coefficient at $p = 4$
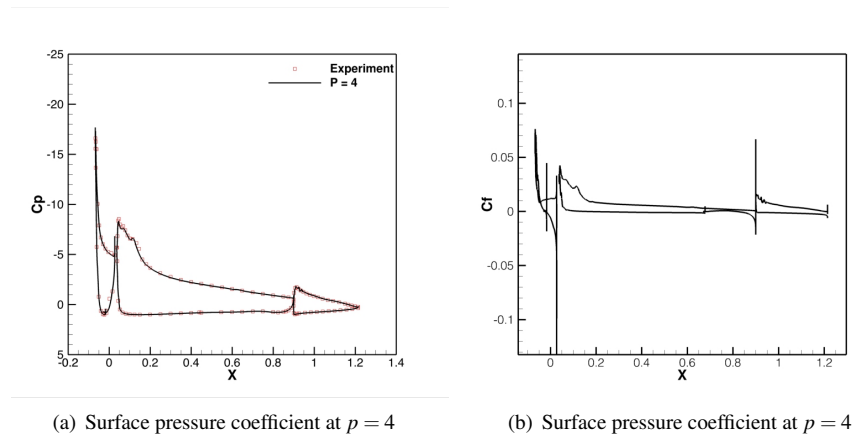
Figure 8: Computed surface pressure and skin friction coefficients using the Spalart-Allmaras turbulence model for flow over the AGARD L1T2 high-lift multi-element airfoil configuration with a discretization order of $p = 4$, $M_\infty = .197$, $\alpha = 20.18^o$, and $Re = 3,520,000$.

Table 2: Computed lift and drag coefficients for the AGARD L1T2 multi-element airfoil configuration at $M_\infty = .197$, $\alpha = 20.18^o$, and $Re = 3,520,000$ using $p = 1$ to $p = 4$

p	NDoF	C_L	C_D
1	265,311	4.055891	0.067782
2	553,707	4.049804	0.066554
3	945,930	4.048049	0.066471
4	1,441,980	4.047551	0.066402

Seventh International Conference on
Computational Fluid Dynamics (ICCFD7),
Big Island, Hawaii, July 9-13, 2012

ICCFD7-4202

Figure 6 depicts the iterative convergence of the $p = 4$ discretization, illustrating that it is far from trivial to converge this flow to steady-state. The oscillations in the residual indicate that minor unsteady flow features may exist in this solution. However, the residual is converged over 10 orders of magnitude, which is sufficient to report approximate lift and drag values, even at $p = 4$. Figure 7(a) and Figure 7(b) depict the Mach number and eddy viscosity contours for a $p = 4$ solution respectively. From the computed Mach number contours the flow is seen to approach sonic conditions on the slat leading-edge upper surface. The DG solver is robust enough to compute this flow without any form of artificial diffusion or limitation. Figure 8(a) shows a comparison between computed surface pressure coefficients and experimental values. The computed surface pressure coefficient results agree well with experimental values throughout the airfoil sections. Figure 8(b) depicts the computed skin friction coefficient using a $p = 4$ DG discretization and a smooth skin friction profile is obtained with the exception of the geometry slope discontinuities. Table 2 provides the numerical values of the computed lift and drag coefficients for each discretization order p. Table 2 shows that the computed drag coefficient is resolved to within less than 1 count and the computed lift coefficient is resolved to within 5 counts. Figure 9(a) depicts the streamlines around the L1T2 multi-element airfoil configuration, showing the high flow incidence angle and high overall streamline curvature over the configuration. Figure 9(b) shows the streamlines near the slat for this case, illustrating the high streamline curvature in this region as the flow is accelerated around the leading edge of the slat and in the gap between the slat and main airfoil. Figure 9(c) shows the streamlines near the flap and flap cove on the main element showing a strong re-circulation region in the flap-cove. The DG solver exhibits no adverse robustness implications as a result of these smooth high gradient phenomena.

(a) Streamlines
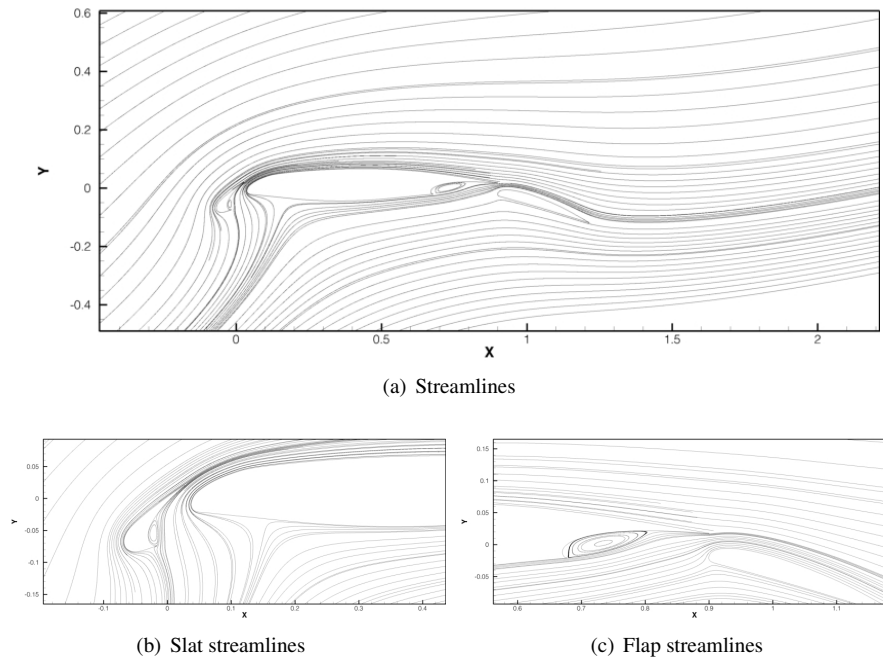

(b) Slat streamlines

(c) Flap streamlines

Figure 9: Streamlines near the slat and flap using the Spalart-Allmaras turbulence model for flow over an L1T2 high lift multi-element airfoil with a discretization order of $p = 4$, $M_\infty = .197$, $\alpha = 20.18^o$, and $Re = 3,520,000$.

5.3   High Lift Multi-element Airfoil: 30P30N

The third test case consists of the turbulent flow over a high-lift multi-element airfoil configuration denoted as the 30P30N configuration. The flow conditions for this test case are $M_\infty = .2$, $\alpha = 16^o$, and $Re = 9,000,000$. The geometry for this test case consists of: a leading edge slat, a center or main element and a trailing edge flap, which are configured for a so-called landing configuration. The computational mesh employed for this case is a mixed-element

Seventh International Conference on
Computational Fluid Dynamics (ICCFD7),
Big Island, Hawaii, July 9-13, 2012

ICCFD7-4202

unstructured mesh consisting of $N = 55,964$ elements shown in Figure 10. The discretization order will be varied from $p = 1$ to $p = 4$.
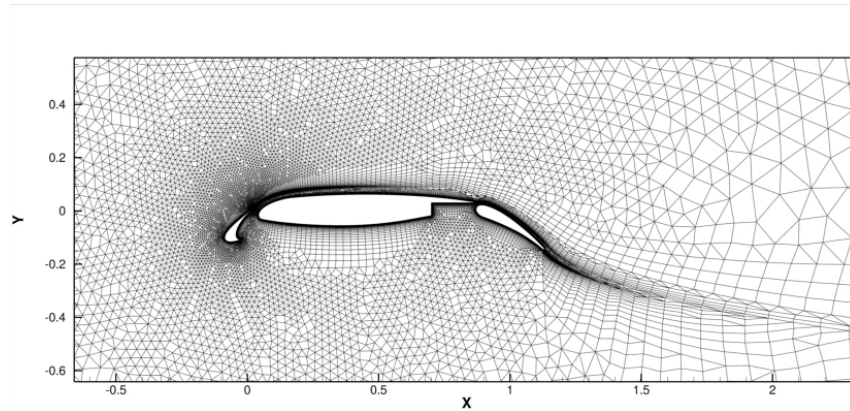

Figure 10: Mixed-element unstructured mesh used for computing flow around the 30P30N high-lift multi-element airfoil configuration at $M_\infty = .2$, $\alpha = 16^o$, and $Re = 9,000,000$.
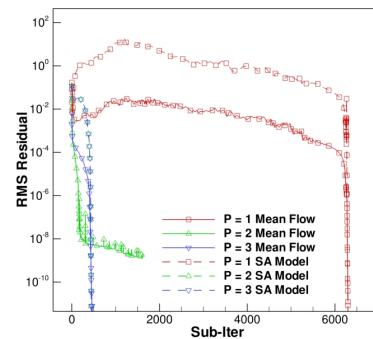

Figure 11: Convergence history for flow over the 30P30N multi-element airfoil configuration using the Spalart-Allmaras turbulence model at $M_\infty = .2$, $\alpha = 16^o$, and $Re = 9,000,000$ for discretization orders $p = 1$ through $p = 3$.

The Mach number and normalized eddy viscosity contours for the $p = 4$ solution are depicted in Figure 12(a) and Figure 12(b) respectively. The computed surface pressure and skin friction coefficients using the present DG solver are depicted along with experimental data[32] in Figure 13(a) and Figure 13(b) respectively. Figure 13(a) and Figure 13(b) show good agreement between the DG solutions and experiment for both the computed surface pressure coefficient and skin friction coefficient. While there is very limited skin friction experimental data available, one should note that the single point of skin friction data on the main element upper surface shows that the DG solver is slightly under predicting the skin friction at this point.

The convergence history for this test case is shown in Figure 11, demonstrating that a fully converged solution is obtained for both the mean flow and SA turbulence model equations up to a discretization order of $p = 3$. The $p = 4$ results are converged approximately 7 orders of magnitude. We hypothesize that at $p = 4$ minor unsteady flow features are developing in the solution, due to the high resolution and low dissipation of the high-order solution, although further investigation is required validate this assumption.

Table 3 gives the discretization order p, N_{DoF}, computed lift and computed drag coefficients for this case. Both the computed lift and drag coefficients vary non-monotonically as the discretization order p is increased. From these results it is difficult to judge the grid convergence of the computed lift and drag coefficients. However, the difference

14

Seventh International Conference on
Computational Fluid Dynamics (ICCFD7),
Big Island, Hawaii, July 9-13, 2012

ICCFD7-4202

(a) Mach number contours, $p = 4$
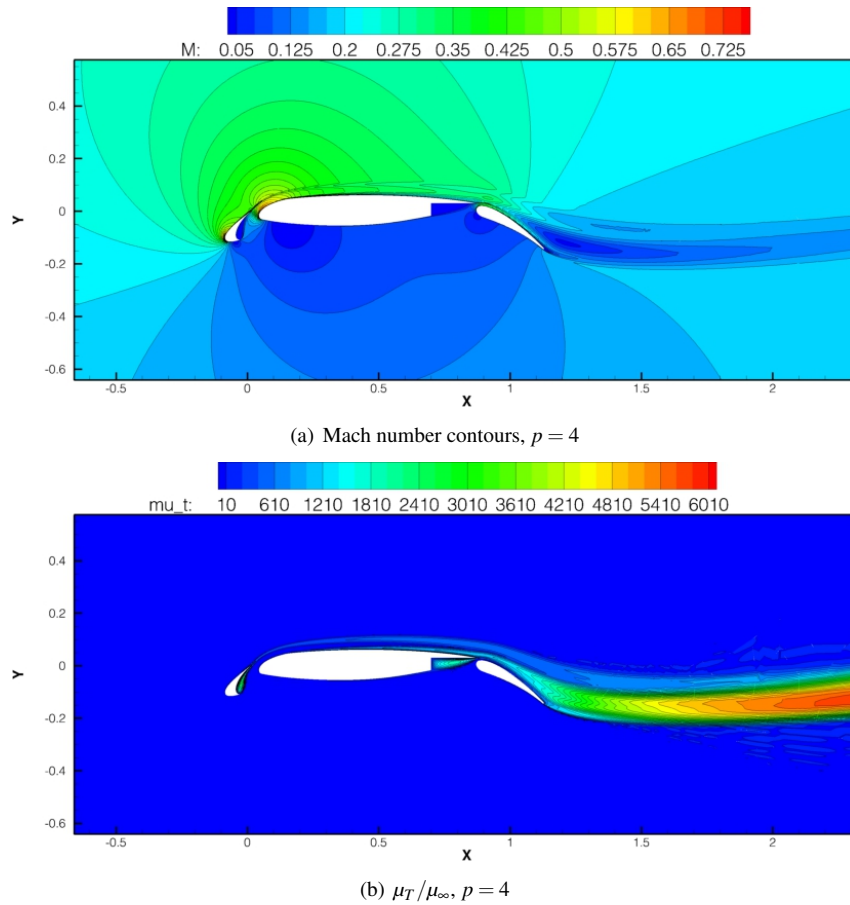

(b) μ_T/μ_∞, $p = 4$

Figure 12: Computed Mach number and eddy viscosity contours using the Spalart-Allmaras turbulence model for flow over the 30P30N multi-element airfoil configuration with, $M_\infty = .2$, $\alpha = 16^o$, and $Re = 9,000,000$ using a discretization order of $p = 4$.

(a) Surface pressure coefficient $p = 1$ to $p = 4$
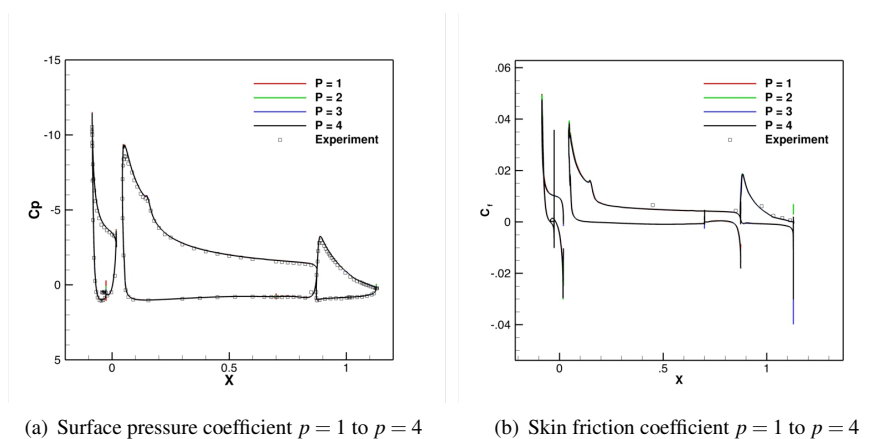

(b) Skin friction coefficient $p = 1$ to $p = 4$

Figure 13: Computed surface pressure and skin friction coefficients using the Spalart-Allmaras turbulence model for flow over the 30P30N multi-element airfoil configuration with discretization orders $p = 1$ to $p = 4$ at $M_\infty = .2$, $\alpha = 16^o$, and $Re = 9,000,000$.

Seventh International Conference on
Computational Fluid Dynamics (ICCFD7),
Big Island, Hawaii, July 9-13, 2012

ICCFD7-4202

Table 3: Computed lift and drag coefficients for the 30P30N multi-element airfoil configuration using discretization orders $p = 1$ to $p = 4$.

p	NDoF	C_L	C_D
1	195,899	4.163636	.050205
2	419,805	4.154856	.051397
3	727,682	4.154760	.050700
4	1,119,530	4.157237	.052103

between the $p = 3$ and $p = 4$ results is 24 counts of lift and 14 counts of drag. The fact that there is more variation in the force coefficients between the $p = 3$ and $p = 4$ solutions compared to the $p = 2$ and $p = 3$ solutions leads to speculation that additional error may have been incurred due to the incomplete convergence of the $p = 4$ solution.

6   Concluding Remarks

The present DG solver has demonstrated the ability to solve high-lift flows robustly by using a modified SA turbulence model definition. The modified SA model is very effective at alleviating the issues encountered with negative values of $\tilde{\nu}$ because when $\tilde{\nu}$ becomes negative the model reverts to an advection only equation which is insensitive the negative values. While the modifications presented in reference[20] increased the robustness of DG discretizations of the SA turbulence model equation, this work has demonstrated that the additional modification to the $\tilde{S}$ term, a fully coupled convective numerical flux function for the RANS-SA system, and making use of a fully coupled Newton solver are additional key components of a robust high-order DG solver for turbulent flows. This work has clearly demonstrated that high-lift flows at high Reynolds numbers can be solved using DG methods. Based on the difficulty of the flow problems considered in this work, DG methods can now be considered robust methods for high-lift flows provided that the appropriate treatment of the turbulence model is employed.

In spite of these successes, significant work remains in the area of high-order accurate RANS simulations. Although the employed turbulence model modifications result in significantly improved robustness, non-smooth and negative turbulence working variable solutions remain. As pointed out in reference[21], this non-smooth solution behavior can adversely impact error estimation and the grid convergence of functional outputs, and complicates the use of hp refinement strategies. Therefore, further turbulence model formulation development will be required to address these issues in a high-order methods framework. Although high-order methods are well suited for large-eddy simulations, most practical problems will require the use of hybrid RANS-LES models and the issues discussed herein will remain important for the near-wall RANS portion of these models.

7   Acknowledgements

References

[1] B. Cockburn and C.-W. Shu. Runge-Kutta discontinuous Galerkin methods for convection-dominated problems. *SIAM J. Sci. Comput.*, 16(3):173–261, 2001.

[2] Li Wang, Dimitri J. Mavriplis, and W. Kyle Anderson. Adjoint sensitivity formulation for discontinuous galerkin discretizations in unsteady inviscid flow problems. *AIAA Journal*, 48(12):2867–2883, Dec 2010.

[3] Brendan S. Mascarenhas, Brian T. Helenbrook, and Harold L. Atkins. Application of p-multigrid to discontinuous galerkin formulations of the euler equations. *AIAA Journal*, 47(5):1200–1208, May 2009.

Seventh International Conference on
Computational Fluid Dynamics (ICCFD7),
Big Island, Hawaii, July 9-13, 2012

ICCFD7-4202

[4] F. Bassi and S. Rebay. Numerical evaluation of two discontinuous galerkin methods for the compressible navier-stokes equations. *Int. J. Numer. Meth. in Fluids*, 40(1):197–207, Sept 2002.

[5] Yidong Xia, Hong Luo, Robert Norgaliev, and Chunpei Cai. A class of reconstructed discontinuous galerkin methods for the compressible flows on arbitrary grids. In *Proceedings of the 49th AIAA Aerospace Sciences Meeting, Orlando FL*, jan 2011. AIAA Paper 2011-199.

[6] Khosro Shahbazi. *A Parallel High-Order Discontinuous Galerkin Solver For The Unsteady Incompressible Navier-Stokes Equations in Complex Geometries*. PhD thesis, University of Toronto, may 2007.

[7] Ralf Hartmann and Paul Houston. Adaptive discontinuous galerkin finite element methods for the compressible euler equations. *Journal of Computational Physics*, 183(2):508–532, Dec 2002.

[8] L. Krivodonova, J. Xin, J.F. Remacle, N. Chevaugeon, and J. Flaherty. Shock detection and limiting with discontinuous galerkin methods for hyperbolic conservation laws. *Appl. Numer. Math*, 48(3-4):323–338, Mar 2004.

[9] Per-Olof Persson and Jaime Peraire. Sub-cell shock capturing for discontinuous galerkin methods. In *Proceedings of 44th Aerospace Sciences Meeting and Exhibit, Reno NV*, jan 2006. AIAA Paper 2006-112.

[10] Francesco Bassi Andrea Crivellini and Stefano Rebay. High-order discontinuous galerkin discretization of transonic turbulent flows. In *Proceedings of the 47th AIAA Aerospace Sciences Meeting, Orlando FL*, Jan 2009. AIAA Paper 2009-180.

[11] Sachin Premasuthan, Chunlei Liang, and Antony Jameson. Computation of flows with shocks using spectral difference scheme with artificial viscosity. In *Proceeding of the 48th Aerospace Sciences Meeting, Orlando, FL*, jun 2010. AIAA Paper 2010-1449.

[12] Garrett E. Barter and David L. Darmofal. Shock capturing with pde-based artificial viscosity for dgfem: Part i. formulation. *Journal of Computational Physics*, 229(5):1810–1827, Mar 2010.

[13] Li Wang and Dimitri J. Mavriplis. Adjoint-based h-p adaptive discontinuous galerkin methods for the 2d euler equations. *Journal of Computational Physics*, 228(20):7643–7661, Nov 2009.

[14] Nicholas K. Burgess and Dimitri J. Mavriplis. An *hp*-adaptive discontinuous galerkin solver for aerodynamic flows on mixed-element meshes. In *Proceeding of the 49th Aerospace Sciences Meeting, Orlando, FL*, Jan 2011. AIAA Paper 2011-490.

[15] Konstantinos Kontzialis and John A. Ekaterinaris. Limiters for discontinuous galerkin discretizations for mixed type meshes with p-type adaptivity. In *Proceedings of the 49th AIAA Aerospace Sciences Meeting, Orlando FL*, jan 2011. AIAA Paper 2011-297.

[16] A. Klöckner, T. Warburton, and J.S. Hesthaven. Viscous shock capturing in a time-explicit discontinuous galerkin method. *Mathematical Modelling of Natural Phenomena*, 6(3):57–83, Jan 2011.

[17] Per-Olof Persson Ngoc Cuong Nguyen and Jaime Peraire. Rans solutions using high order discontinuous galerkin methods. In *Proceeding of the 45th Aerospace Sciences Meeting, Reno, NV*, jan 2007. AIAA Paper 2007-914.

[18] Todd A. Oliver and David L. Darmofal. An unsteady adaptation algorithm for discontinuous galerkin discretizations of the rans equations. In *Proceeding of the 18th AIAA CFD Conference, Miami, FL*, jun 2007. AIAA Paper 2007-3940.

[19] Nicholas K. Burgess, Cristian R. Nastase, and Dimitri J. Mavriplis. Efficient solution techniques for discontinuous galerkin discretizations of the navier-stokes equations on hybrid anisotropic meshes. In *Proceeding of the 48th Aerospace Sciences Meeting, Orlando, FL*, jan 2010. AIAA Paper 2010-1448.

[20] D. Moro, N.C. Nguyen, and J. Peraire. Navier-stokes solution using hybridizable discontinuous galerkin methods. In *Proceeding of the 20th Computational Fluid Dynamics Conference, Honolulu, HW*, Jun 2011. AIAA Paper 2011-3407.

Seventh International Conference on
Computational Fluid Dynamics (ICCFD7),
Big Island, Hawaii, July 9-13, 2012

ICCFD7-4202

[21] Nicholas K. Burgess. *An Adaptive Discontinuous Galerkin Solver for Aerodynamic Flows*. PhD thesis, University of Wyoming, Nov 2011.

[22] P.R. Spalart and S.R. Allmaras. A one-equation turbulence model for aerodynamic flows. *Le Recherche Aerospátiale*, 1:5–21, 1994.

[23] Todd A. Oliver. *A high-order, adaptive, discontinuous Galerkin finite element method for the Reynolds averaged Navier-Stokes equations*. PhD thesis, Massachusetts Institute of Technology, sept 2008.

[24] Nicholas K. Burgess and Dimitri J. Mavriplis. Robust computation of turbulent flows using a discontinuous galerkin method. In *Proceedings of the 50th Aerospace Sciences Meeting, Nashville, TN*, Jan 2012. AIAA Paper 2012-457.

[25] Francesco Bassi, Andrea Crivellini, Stefano Rebay, and Marco Savini. Discontinuous galerkin solution of the reynolds-averaged navier-stokes and k-ω turbulence model equations. *Computers and Fluids*, 34(4):507–540, May 2005.

[26] Ralf Hartmann, Joachim Held, and Tobias Leicht. Adjoint-based error estimation and adaptive mesh refinement for the rans and k-ω turbulence model equations. *Journal of Computational Physics*, 230(11):4268–4284, May 2011.

[27] Walter O. Valarezo and Dimitri J. Mavriplis. Navier-stokes applications to high-lift airfoil analysis. *Journal of Aircraft*, 32(3):618–624, May 1995.

[28] Dimitri J. Mavriplis. Third drag prediction workshop using the nsu3d unstructured mesh solver. *AIAA Journal of Aircraft*, 45(3):750–761, Mar 2008.

[29] Eric J. Nielsen. Fun3d user's manual.

[30] Sherrie L. Krist, Robert T. Biedron, and Christopher L. Rumsey. Cfl3d user's manual (version 5.0). NASA Technical Report 1988-208444, NASA, Jun 1998.

[31] F. Eleuterio Toro. *Riemann Solvers and Numerical Methods for Fluid Dynamics*. Applied Mechanics. Springer-Verlag, New York, NY, 1999.

[32] Steven M. Klausmeyer and John C. Lin. Comparative results from a cfd challenge over a 2d three-element high-lift airfoil. NASA Report 122858, NASA, 1997.